



Article

A Comparison between Kinematic Models for Robotic Needle Insertion with Application into Transperineal Prostate Biopsy

Chiara Zandonà ^{1,*} , Andrea Roberti ^{2,*} , Davide Costanzi ² , Burçin Gül ³, Özge Akbulut ³, Paolo Fiorini ² and Andrea Calanca ²

¹ Department of Computer Science, University of Verona, Strada le Grazie 15, 37134 Verona, Italy

² Department of Engineering for Innovation Medicine, University of Verona, Strada le Grazie 15, 37134 Verona, Italy

³ Department of Engineering and Natural Sciences, Sabanci University, Orta Mahalle-Tuzla, 34956 Istanbul, Turkey

* Correspondence: chiara.zandonà_01@univr.it (C.Z.); andrea.roberti@univr.it (A.R.)

Abstract: Transperineal prostate biopsy is the most reliable technique for detecting prostate cancer, and robot-assisted needle insertion has the potential to improve the accuracy of this procedure. Modeling the interaction between a bevel-tip needle and the tissue, considering tissue heterogeneity, needle bending, and tissue/organ deformation and movement is a required step to enable robotic needle insertion. Even if several models exist, they have never been compared on experimental grounds. Based on this motivation, this paper proposes an experimental comparison for kinematic models of needle insertion, considering different needle insertion speeds and different degrees of tissue stiffness. The experimental comparison considers automated insertions of needles into transparent silicone phantoms under stereo-image guidance. The comparison evaluates the accuracy of existing models in predicting needle deformation.

Keywords: robotic needle insertion; kinematic models; models identification; needle tip prediction; robotic transperineal prostate biopsy



Citation: Zandonà, C.; Roberti, A.; Costanzi, D.; Gül, B.; Akbulut, Ö.; Fiorini, P.; Calanca, A. A Comparison between Kinematic Models for Robotic Needle Insertion with Application into Transperineal Prostate Biopsy. *Technologies* **2024**, *12*, 33. <https://doi.org/10.3390/technologies12030033>

Academic Editor: Jeffrey W. Jutai

Received: 11 January 2024

Revised: 21 February 2024

Accepted: 27 February 2024

Published: 1 March 2024



Copyright: © 2024 by the authors. Licensee MDPI, Basel, Switzerland. This article is an open access article distributed under the terms and conditions of the Creative Commons Attribution (CC BY) license (<https://creativecommons.org/licenses/by/4.0/>).

1. Introduction

One of the main causes of death for men is prostate cancer (PCa), which is the second most common cancer after breast cancer [1]. Epidemiologic studies of prostate cancer have revealed numerous ways in which individual biology and lifestyle factors, such as older age and family history, influence the risk of developing prostate cancer and survival from this disease [1]. Prostate cancer is a clinically heterogeneous disease; some men have an aggressive form, and most others have a slow-growing or indolent form of the disease. The successful treatment of high-risk patients and avoiding overtreatment in low-risk patients depends greatly on early and accurate PCa detection. Needle biopsy is the most reliable technique for detecting PCa and estimating its aggressiveness [2]. The majority of biopsies are performed under ultrasound guidance. A traditional transrectal biopsy can be replaced by a safer transperineal biopsy, which reduces infection risks but may require sedation and must be conducted in an operating room. Robot-assisted needle insertion can improve the accuracy of this procedure, helping to place the tip of the needle safely and accurately without damaging tissues, organs, and vessels. Unfortunately, precise needle placement is difficult to accomplish in real practice because of tissue heterogeneity, needle bending, and tissue/organ deformation and movement. As a result, modeling the interaction between the needle and the tissue is a critical requirement for robotic needle insertion.

During transperineal prostate biopsy, the physician uses ultrasound images to guide the needle from perineum entry points towards the selected target spots [3]. Due to several reasons including economic cost, needles with a bevelled tip are the most commonly used.

Unfortunately, when these needles cross the prostate, they deflect in the tissue due to tissue forces acting on the bevelled tip, producing an unwanted deflection and degrading the accuracy of the system. The advantage of a bevelled tip is that it causes less tissue damage than a symmetric tip and that curved trajectories can be used to avoid delicate tissues, such as bones and blood vessels, which are located between practical entry sites and possible targets. During transperineal prostate biopsy, the surgeon can compensate for the deformation of the needle by twisting the instrument to reach the lesion on the prostate. If we consider robotic automated insertions of the needle for prostate biopsy, needle twisting is not possible, so it is necessary to plan the trajectory from the entry points to the points to be sampled on the organ considering the deformation of the needle and surrounding tissue. Thus, modeling the needle deflection path becomes of paramount importance, and several authors have addressed this topic over the years [4,5]. Previous reports depict three different formalisms to model needle deflection: kinematic models, finite element (FE) models, and quasi-static approximated mechanical models.

In this work, we explore one of these formalisms: kinematic models. A kinematic model for needle insertion was presented for the first time in Park et al. [6]. The authors developed a simple nonholonomic 2D unicycle model to describe how an ideal needle with a bevelled tip moves through a firm tissue. One year later, Webster et al. [7] introduced a nonholonomic 3D bicycle-like model for steering flexible bevelled tip needles. This model describes the same circular arc of the unicycle model but differs when an axial rotation of the needle occurs between two straight insertions. Both models assume that the tissue does not deform. Inserting the needle into stationary tissue causes negligible deformation of the surroundings as the needle bends, so modeling is limited to the motion of the tip. However, if the tissue is not stiff, as the instrument bends, the tissue is compressed. This leads the needle tip to follow a non-circular path. For this reason, Fallahi et al. [8] proposed an extension to the bicycle model of Webster et al. [7]. In this model, the back wheel is replaced with an omnidirectional wheel that can move sideways, allowing the needle to follow a path with a variable radius of curvature.

In this article, we propose an experimental comparison of kinematic models evaluating their accuracy in the context of a transperineal prostate biopsy, considering different needle insertion speeds and different organ stiffnesses. We adapt Fallahi's extended bicycle model to suit our application. To enable a comparative experimental analysis of models, we develop:

1. identification procedures to estimate model parameters,
2. a vision algorithm based on an RGB-D camera system to reconstruct the needle tip position at each insertion step,
3. four transparent phantoms with different degrees of stiffness which allow the use of standard cameras to collect needle insertion frames.

The paper is organised as follows: Section 2 provides the theoretical background on kinematic models and explores in detail the considered models. Section 3 describes the proposed method, including the vision algorithm that recognizes and tracks the needle, the robotic setup and the phantom design. Sections 4 and 5 describe the experimental results and their discussion and Section 6 reports our conclusions and future works.

2. Kinematic Models

The transperineal prostate biopsy procedure consists of straight needle insertion into tissues without twisting. For this reason, the original bicycle model [7] cannot be used in this context because it describes a needle trajectory in a 3D space which is not distinguishable from the unicycle model when limited to a 2D space. Therefore, our comparison considers the unicycle [6] and the extended bicycle models [8]. These models consider a bevelled-tip needle driven by insertion speed v . The tip moves along a path defined by the surrounding material's properties, the geometry of the needle's bevelled tip, and the needle insertion speed. We suppose that the needle is inserted at constant velocity v , measured with respect to the $\{A\}$ frame along the z -axis and without twisting.

2.1. Unicycle Model

The unicycle model considers the needle tip as located at the center of a single wheel (unicycle) lying on the ZY plane as shown in Figure 1. Labels $\{A\}$ and $\{B\}$ represent the global fixed frame and the needle tip frame, respectively.

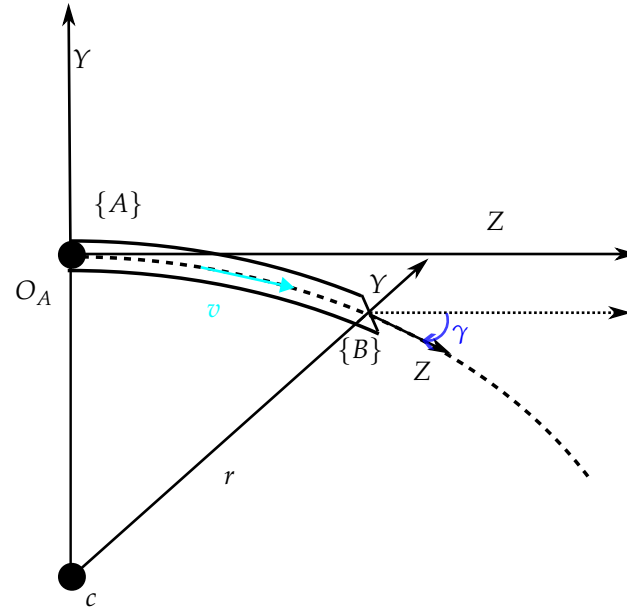


Figure 1. Unicycle model of a flexible needle with a bevelled tip.

According to this model, the needle tip follows a planar path formed by a single arc of fixed curvature with center $c = [0, c_y]$ and radius r , considering entry point O_A at $(0,0)$ in the $\{A\}$ frame. Here, we assume that the needle tip is oriented such that bending occurs toward the negative y -axis as in Figure 1. We let (z, y, γ) define the configuration of the needle tip frame shown in Figure 1, where vector (z, y) is the tip location and γ is the angle between the z -axis of the $\{A\}$ frame and the z -axis of the $\{B\}$ frame that is the needle tip direction. Considering that the needle bends toward the negative y -axis, we have $\gamma \in [-\pi/2, 0]$.

Since the wheel movement satisfies the pure rolling, non-slipping constraint, in the $\{B\}$ frame, the velocity has only the z -axis component, without lateral movements:

$${}^B v_y = 0 \quad (1)$$

where we suppose that wheel speed v_z equals insertion velocity. The dynamic evolution of the needle configuration can be described as

$${}^A \dot{z}(t) = \cos \gamma(t) v_z \quad (2a)$$

$${}^A \dot{y}(t) = \sin \gamma(t) v_z \quad (2b)$$

$${}^A \dot{\gamma}(t) = -\frac{v_z}{r} \quad (2c)$$

with an r constant. Considering O_A the entry point of insertion at $t = 0$, the integration of Equations (2) leads to

$${}^A z(t) = -r \sin \gamma(t) \quad (3a)$$

$${}^A y(t) = c_y + r \cos \gamma(t) \quad (3b)$$

$${}^A \gamma(t) = -\frac{v_z}{r} t \quad (3c)$$

2.2. Extended Bicycle Model

The extended bicycle model [8] considers a bicycle lying on the ZY plane as shown in Figure 2 where labels $\{A\}$, $\{B\}$ and $\{C\}$ denote, respectively, the global fixed frame, the needle tip frame (back wheel) and the front wheel frame. The model consists of two wheels positioned at a fixed distance l from each other with the front wheel oriented at a fixed angle β . The well-known bicycle model with front and back wheels is defined as (z, y, γ) , parameterized by the (z, y) location of the back wheel and the angle of the bicycle body with respect to horizontal γ . The constraints for the front and back wheels are formed by setting the sideways velocity of the wheels to zero. Using the Pfaffian constraints [9], the following dynamical system is obtained:

$$\dot{z} = v_z \cos \gamma \quad (4a)$$

$$\dot{y} = v_z \sin \gamma \quad (4b)$$

$$\dot{\gamma} = \frac{v_z}{l} \tan \beta \quad (4c)$$

with a β constant.

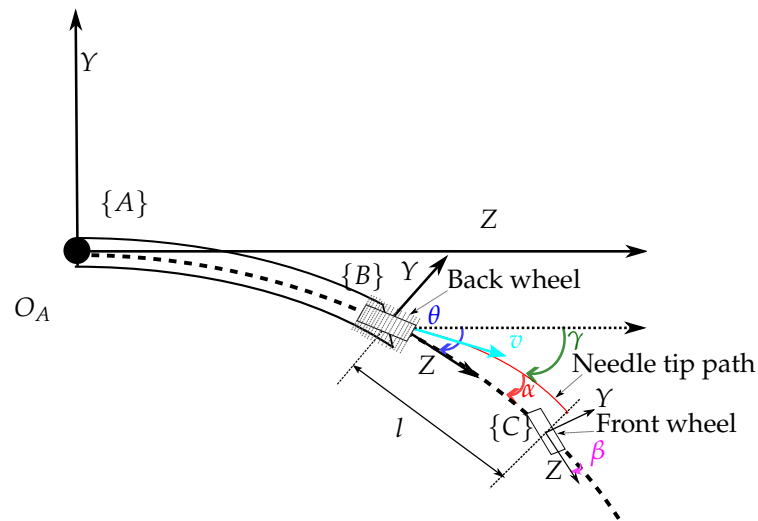


Figure 2. Extended bicycle model of a flexible needle with a bevelled tip.

This model is modified in such a way that when the needle is moving forward into the tissue, lateral movements can happen on the back wheel due to tissue deformation. In this case, the final shape of the needle does not follow the tip path. This model, in contrast to the bicycle model in Equation (4), accounts for this phenomenon by considering an additional state, θ . As for the unicycle model, we suppose that the needle path points toward the negative y -axis starting from entry point O_A . As in the standard bicycle, (z, y, θ) represents the $\{B\}$ frame configuration which is the back wheel body frame. In contrast to the standard bicycle model, the needle tip configuration is (z, y, γ) , where γ is the angle between the z -axis of the $\{A\}$ frame and the needle tip velocity vector ${}^B v$. In practice, γ describes a back wheel slippage phenomenon along the y -axis of the $\{B\}$ frame. If γ defines needle tip velocity with respect to frame $\{A\}$, α defines the same quantity with respect to frame $\{B\}$, and the following relation holds:

$${}^B \alpha = \theta - \gamma \quad (5)$$

As the needle bends toward the negative y -axis, tissue deformation pulls the needle in the opposite direction, so $\alpha \in [-\pi/2, 0]$ and $\gamma \in [-\pi/2, 0]$. The needle tip velocity vector ${}^B v$ and the lateral slipping velocity ${}^B v_y$ are defined as

$${}^B v = v_z + v_y \quad (6a)$$

$${}^B v_y = v_z \tan \alpha \quad (6b)$$

where authors assume α as a quadratic function of γ ,

$${}^B \alpha = \lambda_1 \gamma^2 + \lambda_2 \gamma \quad (7)$$

and λ_i represent tissue-specific parameters related to its mechanical properties. Considering the definition of α as the slippage of the back wheel (Equation (7)), it is clear that for non-zeros λ_1 and λ_2 , the needle path deviates from the constant curvature circular path corresponding to $\lambda_1 = \lambda_2 = 0$. Using the definition of needle tip velocity ${}^B v$ (6a) and angle ${}^B \alpha$ (5), angle ${}^B \theta$ can be expressed as

$${}^B \dot{\theta} = \frac{v_z + v_y}{l} [\tan(\theta - \gamma) + \tan \beta] \quad (8)$$

Considering angle ${}^B \alpha$ (5)–(7), the time variation of angle ${}^B \gamma$, ${}^B \dot{\gamma}$, is calculated as

$${}^B \dot{\gamma} = \dot{\theta} - \dot{\alpha} \quad (9a)$$

$${}^B \dot{\gamma} = \dot{\theta} - \dot{\gamma}(2\lambda_1 \gamma + \lambda_2) \quad (9b)$$

$${}^B \dot{\gamma} = \frac{\dot{\theta}}{1 + 2\lambda_1 \gamma + \lambda_2} \quad (9c)$$

$${}^B \dot{\gamma} = \frac{\dot{\theta}}{1 + \frac{\partial \alpha}{\partial \gamma}} \quad (9d)$$

Finally, the extended bicycle model [8] can be written as

$${}^B \dot{z} = v \cos \gamma \quad (10a)$$

$${}^B \dot{y} = v \sin \gamma \quad (10b)$$

$${}^B \dot{\theta} = \frac{v}{l} [\tan(\theta - \gamma) + \tan \beta] \quad (10c)$$

$${}^B \dot{\gamma} = \frac{\dot{\theta}}{1 + \frac{\partial \alpha}{\partial \gamma}} \quad (10d)$$

3. Method

The experimental comparison is carried out with the setup shown in Figure 3. It consists of a robotic system which performs the insertion with a bevelled tip needle. This system, described in Section 3.4, includes a force sensor on the needle base and an external RGB-D camera. The insertions are performed on phantoms with different degrees of stiffness that emulate the prostate with different tumor levels defined by the Gleason score, which is a grading system for the progress of the tumor. Phantom preparation is described in Section 3.5.

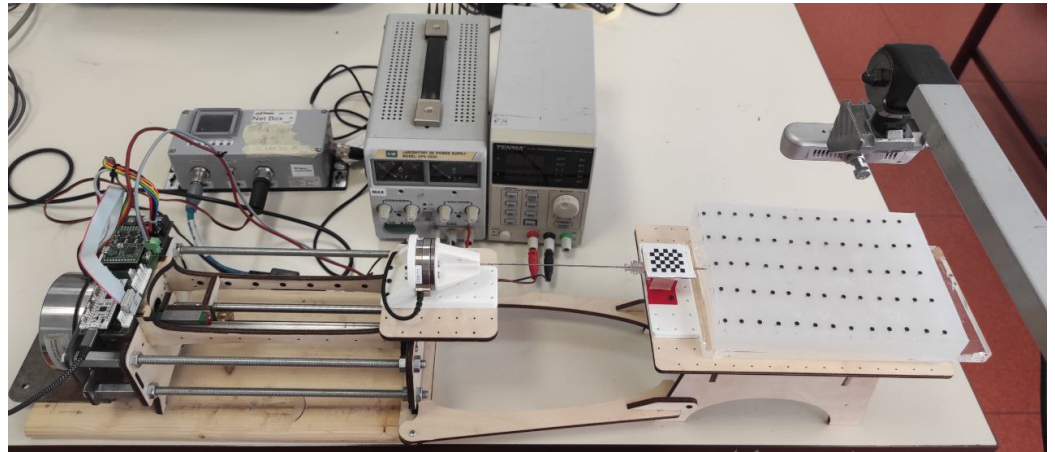


Figure 3. Setup.

A fundamental step of our methodology is to identify the parameters of the unicycle and extended bicycle models to fit needle tip trajectory (Sections 3.1 and 3.2). The trajectory is reconstructed using a vision algorithm (Section 3.3) that identifies and tracks the needle tip throughout its insertion.

3.1. Unicycle Model Identification

This section introduces a methodology to estimate parameters r and c_y for the unicycle model. Given needle tip coordinates ${}^B z(t)$ and ${}^B y(t)$ computed from the vision algorithm (see Section 3.3), these are fitted to the unicycle circumference. The implicit equation of a circumference with a center in $(0, c_y)$ and radius r can be written as

$$z^2(t) + (y(t) - c_y)^2 = r^2 \quad (11)$$

To obtain a formulation suitable for least square regression in the form $\Phi\rho = b$, we rewrite (11) as

$$\underbrace{2y\rho_1 + \rho_2}_{\Phi\rho} = \underbrace{z^2 + y^2}_b \quad (12)$$

where $\rho_1 = c_y$ and $\rho_2 = r^2 - c_y^2$. Then, c_y and r can be easily found.

3.2. Extended Bicycle Model Identification

The authors of [8] introduced a methodology to estimate the parameters of the extended bicycle model: β and l in (8) and λ_1, λ_2 in (7). From the needle tip trajectory (z, y) , computed from the vision algorithm in Section 3.3, it is possible to measure the γ angle as the orientation of needle tip velocity in the $\{A\}$ frame:

$$\gamma = \sin^{-1}\left(\frac{\Delta y}{\Delta d}\right) = \tan^{-1}\left(\frac{\Delta y}{\Delta z}\right) \quad (13)$$

where Δy , Δz , and Δd denote, respectively, the variations of needle tip deflection, insertion, and depth between two sample times. In this context, depth refers to the Euclidean distance in the ZY plane between two successive tip positions. Angle θ is not directly measurable, but its time variation can be expressed in two different formulations, leading to

$$\dot{\theta} = \frac{v}{l}(\tan(\lambda_1\gamma^2 + \lambda_2\gamma) + \tan\beta) \quad (14a)$$

$$\dot{\theta} = \dot{\gamma}\left(1 + \frac{\partial\alpha}{\partial\gamma}\right) = \dot{\gamma}(1 + 2\lambda_1\gamma + \lambda_2) \quad (14b)$$

where (14a) is obtained from (8) substituting (7) while (14b) is calculated from (10d) considering (7). We combine (14a) and (14b) to obtain

$$-2l\lambda_1\gamma\frac{\dot{\gamma}}{v} - l\lambda_2\frac{\dot{\gamma}}{v} - l\frac{\dot{\gamma}}{v} + \tan\beta + \tan(\lambda_1\gamma^2 + \lambda_2\gamma) = 0 \quad (15)$$

which is a function of parameters and known quantities. Known quantities are γ , (13), its time variation $\dot{\gamma}$ and the needle tip speed v . Unknown parameters are l , β , λ_1 , and λ_2 , and they can be identified by a non-linear least square regression algorithm as proposed by the authors [8]. Unfortunately, the objective function presents several local minima and, to improve the results, the following constraints are imposed:

$$l \in [0, 2] \quad (16a)$$

$$\beta \in [-\frac{\pi}{2}, 0] \quad (16b)$$

$$\lambda_1 \in [-1, 1] \quad (16c)$$

$$\lambda_2 \in [-1, 1] \quad (16d)$$

Even using such constraints, this methodology, as proposed by the authors [8], is not always able to find an appropriate solution. For this reason, we use a genetic algorithm to minimize the residual error between the experimental data and the predicted ones.

3.3. Needle Recognition and Tracking

To track the needle tip position in each time frame, we used the semantic segmentation module based on the Generative Adversarial Network (GAN) model [10]. Compared to the other models, this network has the advantage of requiring very few RGB samples representing the setup to obtain high-quality results. The GAN consists of two main components: a generator and a discriminator.

- **Generator:** The generator takes an input image, processes it through a neural network, and produces an output image. It learns to create realistic and visually appealing results by mimicking the patterns, textures, and styles found in the training data. As training progresses, the generator becomes increasingly adept at generating images that are indistinguishable from real data.
- **Discriminator:** The discriminator, on the other hand, acts as a critic. It tries to distinguish between real images from the training dataset and fake images generated by the generator. Through adversarial training, the discriminator becomes skilled at identifying flaws or inconsistencies in the generated images.

As training continues, the generator and the discriminator engage in a competitive process, with the generator constantly improving its ability to generate convincing output and the discriminator becoming better at discerning real from fake. This dynamic equilibrium ultimately results in the generator producing high-quality, pixel-to-pixel output that retains the essential characteristics of the input data.

Figure 4 shows an example of segmentation of an image acquired from the realsense camera. The classes corresponding to objects in the scene are encoded following Table 1.

Table 1. Semantic Scene Color Encoding.

Color	Semantic Meaning
	Background
	Needle
	Markers
	Tissue

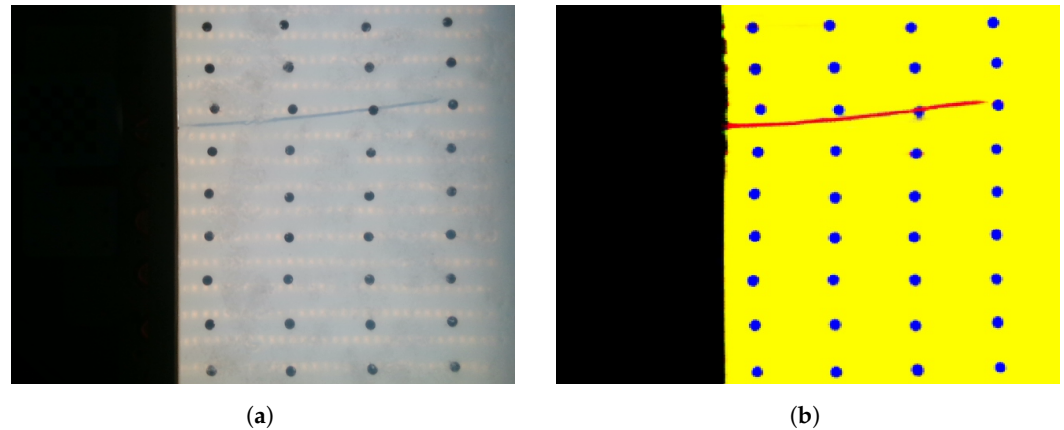


Figure 4. An example of real-time semantic segmentation computed with the Realsense camera. (a) Realsense view; (b) Segmented image.

Once we obtained the segmented image, we defined the workspace by placing a chessboard over a 3D-printed support where the needle passes through. This allowed us to retrieve the pixel/millimeter ratio that is needed to have the needle position in the 3D metric space. Starting from the pose of the chessboard, we filtered out an area of interest around the needle path and created a bounding box in the semantic image, and then worked with a smaller image. Finally, we segmented the needle from the semantic image and then extracted the center point of the needle tip as shown in Figure 5, which was used later for model estimation.



Figure 5. An example frame with the needle tip estimation represented as a red dot.

The coordinates (z, y) of the needle tip, which are derived from the mask obtained through semantic segmentation for each frame, were individually subjected to a third-order polynomial fitting process over time-to-position data in order to mitigate measurement noise.

3.4. Experimental Setup

We design a robotic system to perform insertion experiments into tissues, with one degree of freedom (DoF) capable of translational motion along the needle's principal axis. A mechanical drive system pushes the needle into the phantom using a direct drive motor (model EC90flat) and a worm gear system. The trajectory of the needle tip is reconstructed using an Intel RealSense d435 camera positioned approximately 20 cm from the surface of the phantom, operating at a rate of 30 Hz to capture the images fed into the vision algorithm. The use of transparent phantoms and a camera allows us to acquire the entire needle tip trajectory during the insertion with good accuracy, which is something ultrasound imaging cannot afford due to its noise.

The needle bevel tip is oriented so that the needle deflection plane ZY is parallel to the imaging plane. In the experiments, a standard 18-gauge brachytherapy needle with a bevel angle of 15° is used. The insertions are carried out at various constant velocities to a depth of 100 mm.

3.5. Phantom Design

In our comparative experiment, we evaluate four transparent phantoms with varying stiffness values (30, 50, 70, 100 kPa), covering the range associated with both benign and malign conditions of the prostate gland [11,12]. Two-component silicone elastomers (SL

3358 A and SL 3358 B, KCC Corporation, Korea) were utilized in equal amounts for the preparation of the phantom. Silicone oil (G Line T100, KCC Corporation, Korea) in differing amounts (50, 55.5, 66.6) and 0.03 wt% cotton fibers were added to the silicone mixture to adjust the stiffness of the model and simulate the fibrous and muscular tissue of the prostate. The preparation of the first layer of the phantom body with fibers (2.5 cm height) was followed by the insertion of 65 pin markers (13 × 5 rows) positioned at the required locations (Figure 6a). Subsequently, the final layer of the phantom (0.5 cm height) with fibers was produced by curing the silicone formulation that is equivalent to the bottom layer. Each layer was cured separately at 70 °C in an oven for 100 min (20 cm × 14 cm × 3 cm) (Figure 6b).

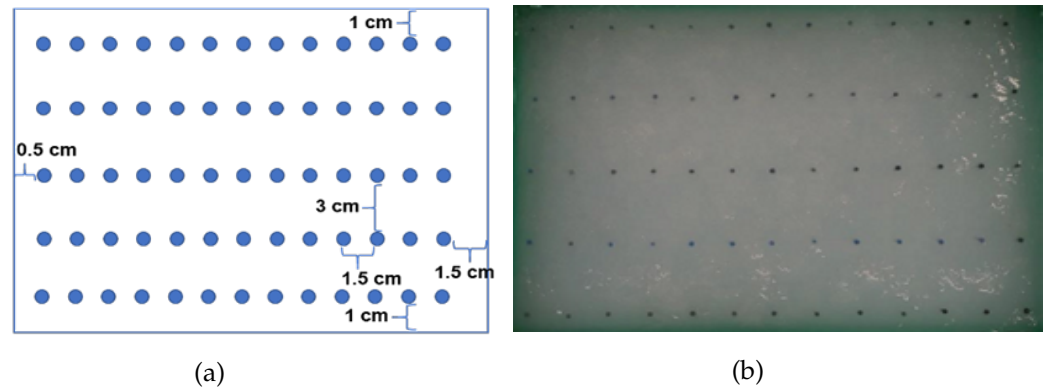


Figure 6. (a) The sketch of the prostate phantom and the markers; (b) the view of the prostate phantom from the top.

3.6. Mechanical Characterization

Different formulations of the two-component silicone elastomers with silicone oil and cotton fiber supplements were prepared in dog bone shape according to the American Society for Testing and Materials International (ASTM) standards. The specimens were tested with 200 N force using the Universal Testing Machine (UTM) (Zwick/Roell), and an average of three tests were reported (Figure 7).

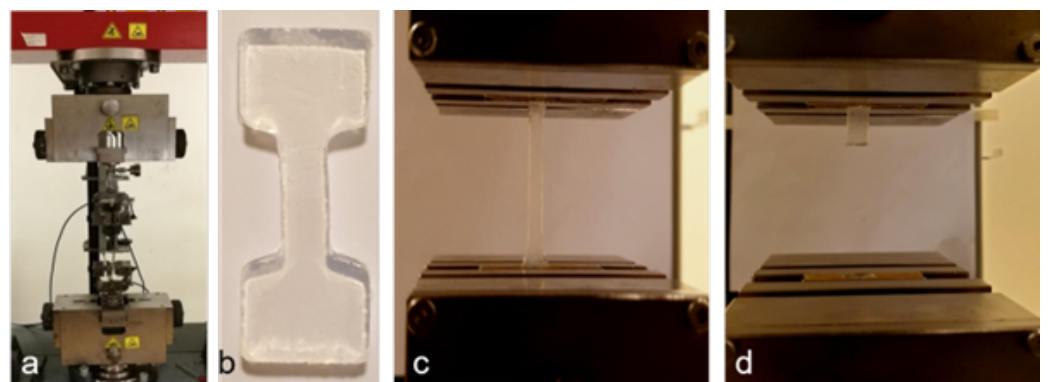


Figure 7. (a) The mechanical property measurement setup in Zwick/Roell UTM, (b) silicone sample prepared in dog-bone shape, and the image of the silicone sample (c) during the tensile test and (d) at the end of the test (fracture).

The degrees of stiffness were adjusted with the addition of silicone oil and supplementary materials (e.g., cotton fibers) to reach the highest resemblance to the reported values of the prostate tissue. The stiffness of the phantom body range was between 32.8 and 107 kPa (Figure 8).

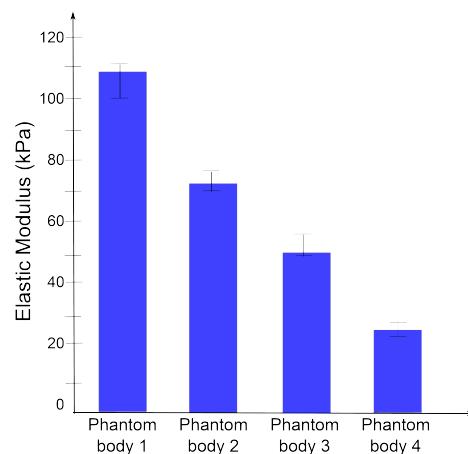


Figure 8. The stiffness of the different silicone-based prostate model formulations with supplements that are utilized in the design of the phantom body.

4. Experimental Results

Using the robotic setup, the needle is inserted to a depth of 100 mm considered to be the longest distance between the perineum and the apex of the prostate. Insertions are performed at two different velocities (10, 20 mm/s). For each stiffness and velocity pair, we perform four repetitions. We perform model identification procedures using data from the first three repetitions, and we use the fourth repetition to assess the prediction accuracy of the models. The unicycle model and the extended bicycle model are labeled, respectively, as $M1$ and $M2$. Results in Tables 2 and 3 show, respectively, the average final tip deflection $\omega_{exp}(l)$ with the standard deviation of the final tip position σ_{exp} and the average tip error identification for unicycle model e_{meanM1} and extended bicycle model e_{meanM2} with their standard deviations σ_{eM1} and σ_{eM2} for every phantom's stiffness and velocity pair. Figure 9 shows examples of data from identification procedures related to phantoms with stiffness 30 kPa and 100 kPa at velocities 10 $\frac{\text{mm}}{\text{s}}$ and 20 $\frac{\text{mm}}{\text{s}}$.

Table 2. Average final tip deflection and standard deviation considering 8 experimental conditions (4 phantom and 2 velocity pairs) with four repetitions each.

Insertion Velocity [mm/s]	Stiffness [kPa]	$\omega_{exp}(l)$ [mm]	σ_{exp} [mm]
10	30	−8.26	0.43
	50	−10.80	0.95
	70	−12.18	1.13
	100	−12.58	1.11
20	30	−7.65	0.56
	50	−9.51	0.20
	70	−10.57	1.14
	100	−11.78	1.44

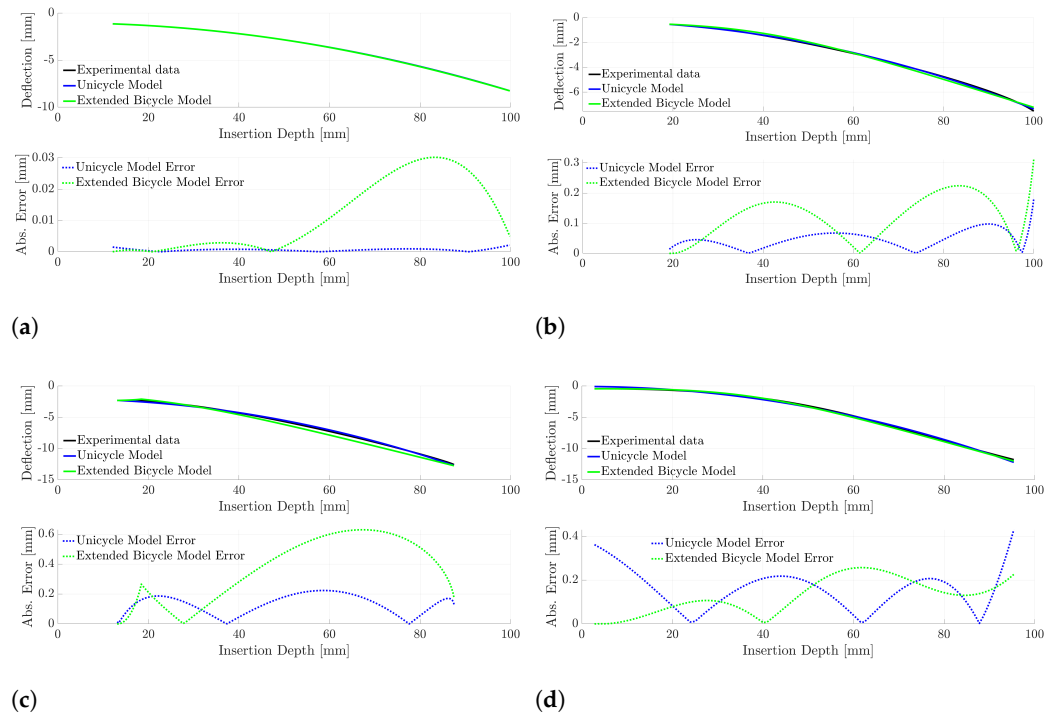


Figure 9. Models identification on needle insertions experiments in the prostate stiffness range (30, 100 kPa) at two different velocities (10, 20 mm/s). (a) Stiffness: 30 kPa, Velocity: 10 mm/s; (b) Stiffness: 30 kPa, Velocity: 20 mm/s; (c) Stiffness: 100 kPa, Velocity: 10 mm/s; (d) Stiffness: 100 kPa, Velocity: 20 mm/s.

Table 3. Average tip error identification and standard deviation for the Unicycle Model and the Extended Bicycle Model considering 8 experimental conditions (4 phantom and 2 velocity pairs) with four repetitions each.

Insertion Velocity [mm/s]	Stiffness [kPa]	e_{meanM1} [mm]	e_{meanM2} [mm]	σ_{eM1} [mm]	σ_{eM2} [mm]
10	30	6.15×10^{-4}	0.012	5.18×10^{-7}	2.52×10^{-4}
	50	0.051	0.065	0.005	0.006
	70	0.056	0.338	0.005	0.156
	100	0.130	0.364	0.020	0.174
20	30	0.053	0.126	0.004	0.022
	50	0.013	0.142	0.022	0.032
	70	0.014	0.151	0.027	0.033
	100	0.153	0.166	0.031	0.034

We estimate the parameters of the models by performing a least square identification for the unicycle model and using a genetic algorithm for the extended bicycle model as described in Sections 3.1 and 3.2. To robustify the identification procedure, the estimated parameters are averaged considering data from the three insertions. To access the models' accuracy, the simulated needle trajectory is compared to experimental data of the fourth repetition.

Results in Table 4 show the maximum tip prediction error for unicycle model e_{maxM1} and extended bicycle model e_{maxM2} and their root-mean-squared errors (RMSEs) $RMSE_{M1}$ and $RMSE_{M2}$ for every phantom's stiffness and velocity pair. Figure 10 shows examples of data from prediction procedures related to phantoms with stiffness 30 kPa and 100 kPa at velocities $10 \frac{\text{mm}}{\text{s}}$ and $20 \frac{\text{mm}}{\text{s}}$.

Table 4. Maximum tip prediction error and the root-mean-squared error (RMSE) for Unicycle Model e_{maxM1} and Extended Bicycle Model e_{maxM2} considering 8 experimental conditions (4 phantom and 2 velocity pairs) with four repetitions each.

Insertion Velocity [mm/s]	Stiffness [kPa]	e_{maxM1} [mm]	e_{maxM2} [mm]	$RMSE_{M1}$ [mm]	$RMSE_{M2}$ [mm]
10	30	0.18	0.77	0.11	0.49
	50	0.32	0.45	0.26	0.27
	70	0.43	2.07	0.31	0.76
	100	0.44	1.04	0.28	0.71
20	30	0.20	0.61	0.12	0.19
	50	0.22	0.45	0.18	0.26
	70	0.29	0.78	0.19	0.33
	100	0.75	1.24	0.29	0.85

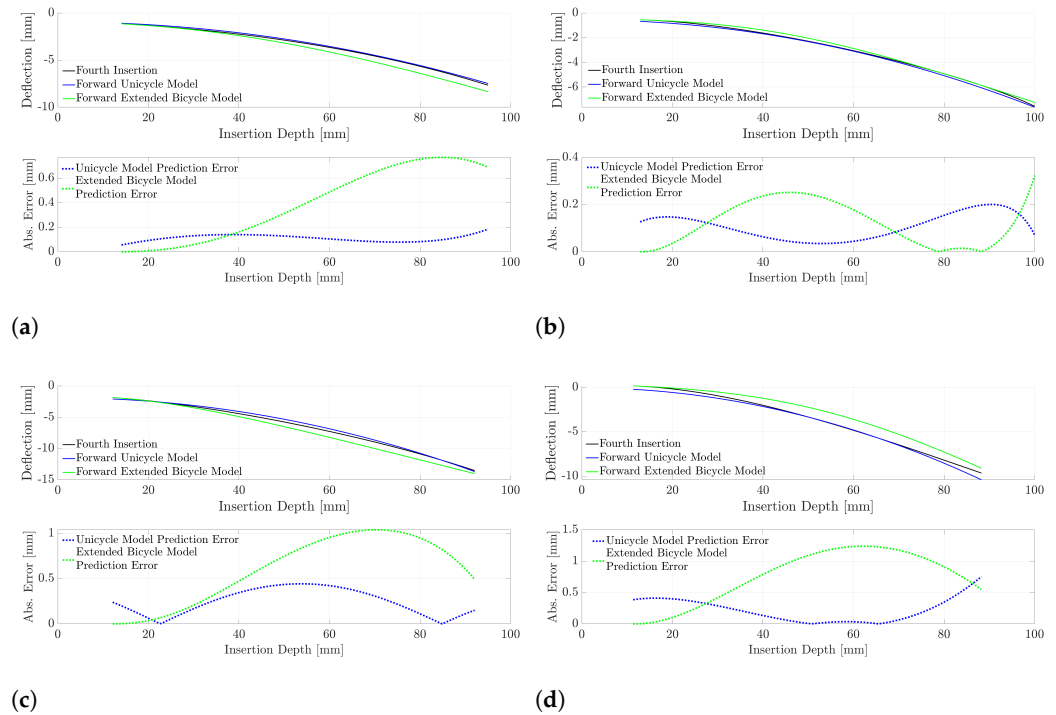


Figure 10. Unicycle and Extended Bicycle Model prediction on the fourth needle insertion experiment. (a) Stiffness: 30 kPa, Velocity: 10 mm/s; (b) Stiffness: 30 kPa, Velocity: 20 mm/s; (c) Stiffness: 100 kPa, Velocity: 10 mm/s; (d) Stiffness: 100 kPa, Velocity: 20 mm/s.

5. Discussion

From Table 2, one can notice that insertions exhibit a notable final displacement, around 10% of their whole length, and this motivates the use of models for the prediction of needle deflection. From Table 4, one can observe that both models are quite accurate in predicting the tip's final position. In terms of RMSE, we achieved a tenth of a millimetre accuracy down to the millimetre (in the case of more rigid phantom insertions). The maximum errors were less than or equal to 0.75 mm for the unicycle model and less or equal to 2.07 mm for the extended bicycle model. In spite of its lower complexity, the unicycle model is more accurate than the extended bicycle model. Both in terms of RMSE and maximum error, the unicycle model is, on average, 2.5 times more accurate than the extended bicycle model. In any experimental scenario, the unicycle model generates smaller errors than the extended bicycle model (for each stiffness and velocity pair). For both models, higher errors in predicting the final needle tip deflection were obtained when the needle was pushed into

the more rigid phantoms (70 and 100 kPa) at the highest velocity ($20 \frac{\text{mm}}{\text{s}}$). Since the unicycle model is a linear regression identification, it is faster and requires less computational effort than the extended bicycle model. We measured an average computation time of 0.7 ms for the unicycle model and 45 s (range 20–65 s, executed on Intel Core i7-6700HQ processor running four threads) for the extended bicycle model as a final remark.

6. Conclusions

This work compares the kinematic models for robotic needle insertion targeting straight needle insertion as in transperineal prostate biopsy. Our experimental comparison considers four transparent phantoms with increasing stiffness simulating fibrous and muscular prostate tissue in benign and malignant disease conditions. Experimental results show that, in spite of its simplicity, the unicycle model outperforms the extended bicycle model in terms of accuracy and computational time. Modeling the deformation of the needle and the surrounding tissue during insertion into the prostate allows surgeons to take samples accurately from the organ, thus ensuring the accurate identification of prostate cancer and indicating the level of risk for the patient. Prostate biopsy is one of the most impactful and independent parameters that direct physicians to the surgery if it is not possible to follow other treatments. In this comparative study of kinematic models, the tissue is considered rigid or with small deformation, allowing modeling of the deflection of the needle without necessarily considering the forces of interaction with the tissue. However, heterogeneous tissues with different stiffness levels are crossed in the transperineal biopsy procedure. In our future work, we will evaluate non-straight needle insertions, including more complex models such as virtual spring mechanical models [13,14] and finite element models [15–17] and the influence of skin tension, subcutaneous fat, and pelvic diaphragm will be considered to evaluate the targeting error in a complete robotic needle insertion procedure.

Author Contributions: Conceptualization, C.Z., A.R., D.C. and A.C.; methodology, C.Z. and A.R.; software, C.Z. and A.R.; validation, C.Z. and A.R.; formal analysis, C.Z.; investigation, C.Z.; resources, C.Z., A.R. and B.G.; data curation, C.Z. and A.R.; writing—original draft preparation, C.Z. and A.R.; writing—review and editing, C.Z., A.R., B.G., Ö.A. and A.C.; visualization, C.Z.; supervision, A.C.; project administration, P.F.; funding acquisition, A.C. and P.F. All authors have read and agreed to the published version of the manuscript.

Funding: This project received funding from the European Research Council (ERC) under the European Unions Horizon 2020 research and innovation programme under grant agreement No. 742671 (ARS).

Institutional Review Board Statement: Not applicable.

Informed Consent Statement: Not applicable.

Data Availability Statement: The data will be available upon reasonable request from the corresponding authors.

Conflicts of Interest: The authors declare no conflicts of interest.

References

1. Pernar, C.H.; Ebot, E.M.; Wilson, K.M.; Mucci, L.A. The Epidemiology of Prostate Cancer. *Cold Spring Harb. Perspect. Med.* **2018**, *8*, a030361. [[CrossRef](#)] [[PubMed](#)]
2. Verma, S.; Choyke, P.L.; Eberhardt, S.C.; Oto, A.; Tempany, C.M.; Turkbey, B.; Rosenkrantz, A.B. The Current State of MR Imaging-targeted Biopsy Techniques for Detection of Prostate Cancer. *Radiology* **2017**, *285*, 343–356. [[CrossRef](#)] [[PubMed](#)]
3. Maris, B.; Tenga, C.; Vicario, R.; Palladino, L.; Murr, N.; De Piccoli, M.; Calanca, A.; Puliatti, S.; Micali, S.; Tafuri, A.; et al. Toward autonomous robotic prostate biopsy: A pilot study. *Int. J. Comput. Assist. Radiol. Surg.* **2021**, *16*, 1393–1401. [[CrossRef](#)] [[PubMed](#)]
4. DiMaio, S.P.; Salcudean, S.E. Needle insertion modeling and simulation. *IEEE Trans. Robot. Autom.* **2003**, *19*, 864–875. [[CrossRef](#)]
5. Simone, C.; Okamura, A.M. Modeling of needle insertion forces for robot-assisted percutaneous therapy. In Proceedings of the 2002 IEEE International Conference on Robotics and Automation, Washington, DC, USA, 11–15 May 2002; Volume 2, pp. 2085–2091.

6. Park, W.; Kim, J.S.; Zhou, Y.; Cowan, N.; Okamura, A.; Chirikjian, G. Diffusion-Based Motion Planning for a Nonholonomic Flexible Needle Model. In Proceedings of the 2005 IEEE International Conference on Robotics and Automation, Barcelona, Spain, 18–22 April 2005; pp. 4600–4605. [[CrossRef](#)]
7. Robert, J.; Webster, I.; Kim, J.S.; Cowan, N.J.; Chirikjian, G.S.; Okamura, A.M. Nonholonomic Modeling of Needle Steering. *Int. J. Robot. Res.* **2006**, *25*, 509–525. [[CrossRef](#)]
8. Fallahi, B.; Khadem, M.; Rossa, C.; Sloboda, R.; Usmani, N.; Tavakoli, M. Extended bicycle model for needle steering in soft tissue. In Proceedings of the 2015 IEEE/RSJ International Conference on Intelligent Robots and Systems (IROS), Hamburg, Germany, 28 September–2 October 2015; pp. 4375–4380. [[CrossRef](#)]
9. Murray, R.M.; Sastry, S.S.; Zexiang, L. *A Mathematical Introduction to Robotic Manipulation*, 1st ed.; CRC Press, Inc.: Boca Raton, FL, USA, 1994.
10. Isola, P.; Zhu, J.Y.; Zhou, T.; Efros, A.A. Image-to-Image Translation with Conditional Adversarial Networks. In Proceedings of the 2017 IEEE Conference on Computer Vision and Pattern Recognition (CVPR), Honolulu, HI, USA, 21–26 July 2017.
11. Hungr, N.; Long, J.A.; Beix, V.; Troccaz, J. A realistic deformable prostate phantom for multimodal imaging and needle-insertion procedures. *Med. Phys.* **2012**, *39*, 2031–2041. [[CrossRef](#)] [[PubMed](#)]
12. Ji, Y.; Ruan, L.; Ren, W.; Dun, G.; Liu, J.; Zhang, Y.; Wan, Q. Stiffness of prostate gland measured by transrectal real-time shear wave elastography for detection of prostate cancer: A feasibility study. *Br. J. Radiol.* **2019**, *92*, 20180970. [[CrossRef](#)] [[PubMed](#)]
13. Glozman, D.; Shoham, M. Flexible needle steering and optimal trajectory planning for percutaneous therapies. In Proceedings of the 7th International Conference on Medical Image Computing and Computer-Assisted Intervention–MICCAI 2004, Saint-Malo, France, 26–29 September 2004; Springer: Berlin/Heidelberg, Germany, 2004; pp. 137–144.
14. Glozman, D.; Shoham, M. Image-guided robotic flexible needle steering. *IEEE Trans. Robot.* **2007**, *23*, 459–467. [[CrossRef](#)]
15. Alterovitz, R.; Goldberg, K.; Okamura, A. Planning for steerable bevel-tip needle insertion through 2D soft tissue with obstacles. In Proceedings of the 2005 IEEE International Conference on Robotics and Automation, Barcelona, Spain, 18–22 April 2005; pp. 1640–1645.
16. Alterovitz, R.; Lim, A.; Goldberg, K.; Chirikjian, G.S.; Okamura, A.M. Steering flexible needles under Markov motion uncertainty. In Proceedings of the 2005 IEEE/RSJ International Conference on Intelligent Robots and Systems, Edmonton, AB, Canada, 2–6 August 2005; pp. 1570–1575.
17. Dehghan, E.; Salcudean, S.E. Needle insertion parameter optimization for brachytherapy. *IEEE Trans. Robot.* **2009**, *25*, 303–315. [[CrossRef](#)]

Disclaimer/Publisher’s Note: The statements, opinions and data contained in all publications are solely those of the individual author(s) and contributor(s) and not of MDPI and/or the editor(s). MDPI and/or the editor(s) disclaim responsibility for any injury to people or property resulting from any ideas, methods, instructions or products referred to in the content.